LUT University

Localization of dielectric breakdown defects in multilayer ceramic capacitors using 3D X-ray imaging

Ingman Jonny, Jormanainen Joni, Vulli Aleksi, Ingman Jimmy, Maula Kari, Kärkkäinen Tommi, Silventoinen Pertti

Please cite the publication as follows:

Ingman, J.M., Jormanainen, J.P.A., Vulli, A.M., Ingman, J.D., Maula, K., Kärkkäinen, T.J., Silventoinen, P. (2018). Localization of dielectric breakdown defects in multilayer ceramic capacitors using 3D X-ray imaging. Journal of the European Ceramic Society. DOI:10.1016/j.jeurceramsoc.2018.10.030

J.M. Ingman [a,b*], J.P.A. Jormanainen [a], A.M. Vulli [a], J.D. Ingman [a,b], K. Maula [a], T.J. Kärkkäinen [b] P. Silventoinen [b]

[a] ABB Oy, Hiomotie 13, P.O. Box 184, 00381 Helsinki, Finland

[b] Lappeenranta University of Technology, LUT School of Energy systems, Skinnarilankatu 34, 53850 Lappeenranta, Finland

Localization of dielectric breakdown defects in multilayer ceramic capacitors using 3D X-ray imaging

Abstract

In this article, a non-destructive method using 3D X-ray imaging to find dielectric breakdown defects in multilayer ceramic capacitors (MLCCs) aged by high temperature and high voltage in an accelerated test is presented. In total, 64 aged samples were investigated using 2D X-ray imaging and half of them were further analysed with 3D X-ray imaging. Miniscule dielectric breakdown defects located in the MLCC active region are extremely difficult to identify solely using cross-section analysis or 2D X-ray imaging. In this study, the information provided by the 3D X-ray analysis was used to localize the defects for cross-section analysis. Cross-section analysis was performed to verify the dielectric breakdowns and their locations. 3D X-ray imaging is an effective method for detecting dielectric breakdown defects in MLCCs due to its short analysis time and high accuracy. This further facilitates failure analysis processes by providing the required grinding depth in cross-section analysis procedures.

1. Introduction

Multilayer ceramic capacitors are widely used in electronic products [1] due to their small size. In addition, with the current trend of miniaturization in electronics [2] to reach even higher volumetric efficiency [3], the thickness active dielectric layer has decreased into the micron or submicron range. Consequently, MLCCs have become more vulnerable to dielectric breakdowns because of the reduced insulation resistance [4]. Hence, the thickness of the dielectric layer and the number of stacking grains have been found to be crucial to the reliability of MLCCs [5].

Dielectric breakdown is one of the most common failure mechanisms in multilayer ceramic capacitors [6]. In this particular failure mechanism, areas in the dielectric material start to experience self-heating due to local increases in leakage current, which in turn further increases the leakage current [7]. As a consequence, the insulation resistance of the dielectric deteriorates and eventually a conductive path between neighbouring electrodes is created, resulting in complete dielectric breakdown.

For MLCCs with base metal electrodes, Weachock and Liu [8] have reported three distinct dielectric breakdown failure modes: *avalanche breakdown*, *thermal runaway*, and *slow degradation*. Avalanche breakdown and thermal runaway have been referred to as "catastrophic" failures, where the thermal breakdown void region is surrounded by transverse cracks that extend through several layers of electrodes. In slow degradation, the stoichiometry of barium titanate (BaTiO$_3$) grains is changed, causing local melting of the dielectric grains and the formation of small cracks extending between the anode and the cathode electrodes. As a result, nickel dissolves along the cracks, eventually leading to a resistive short. In Weachock and Liu's study, most of the MLCCs were observed to fail in a two-stage dielectric wear-out, starting with a slow degradation followed by a thermally dominated catastrophic breakdown.

* Corresponding author.
  E-mail address: jonny.ingman@fi.abb.com (J.M. Ingman).

Accelerated tests with overstress have been utilized to quickly induce the aforementioned failure modes in multilayer ceramic capacitors [9-11]. Typically, these failure modes have been studied by cross-sectioning the tested samples in order to reveal the locations of dielectric breakdowns for failure analysis. The disadvantage of this method is that any flaw in the sample preparation process can easily destroy evidence of the small defects. Furthermore, it is often quite time-consuming and challenging to find the location of the dielectric breakdown solely by cross-sectioning.

In this study, we demonstrate a novel non-destructive approach for detecting dielectric breakdowns in MLCCs with 3D X-ray imaging. To induce dielectric breakdown due to melting of both the dielectric and nickel electrodes, MLCCs with base metal electrodes were subjected to high voltage and high temperature. It has been shown that 2D X-ray imaging can be used successfully in investigating cracks in multilayer ceramic capacitors [12]. The aged samples were therefore analysed using both 2D and 3D X-ray imaging, of which only the latter could be used to detect the dielectric breakdown defects directly. Additionally, cross-section analysis was performed to verify the dielectric breakdown locations obtained from the 3D X-ray analysis. The locations obtained with 3D X-ray imaging greatly facilitated the cross-section preparation by providing the grinding depth and hence minimizing the loss of evidence during the analysis process. Furthermore, it was noted that 3D X-ray imaging is faster than, and at least as accurate a method of detecting dielectric breakdowns in MLCCs as, cross-section analysis.

Dielectric breakdowns have been discussed in multiple studies; however, the distribution of the defect locations has not been reported so far. With 3D X-ray, the distribution of defects inside an MLCC of a selected sampling can be assessed by combing the location information for defects. The defect locations analysed in this study were found to be randomly distributed within the MLCCs. Using 3D X-ray imaging to detect defects may allow future research to compare defect distributions of different MLCC manufacturers and/or batches to reveal weak spots.

2. Methods

2.1. Test setup

A test setup was designed and built to induce dielectric breakdown of MLCCs. The schematic diagram and general design of the printed circuit board (PCB) for the accelerated test is shown in **Error! Reference source not found.**. The devices under test (DUT) – C_1 to C_{32} in the figure – were assembled on eight PCBs, and each test PCB was designed to support 32 MLCCs with accompanying 100 mA fast-acting fuses. The current limit of the DC power supply was adjusted to be 30 times the rated value of the fuse. In the event of capacitor short circuit, the fuse opens, whereby the data acquisition (DAQ) input voltage changes from zero to the Zener voltage. The time-to-failure is recorded by the DAQ utilizing a custom-made LabVIEW application.
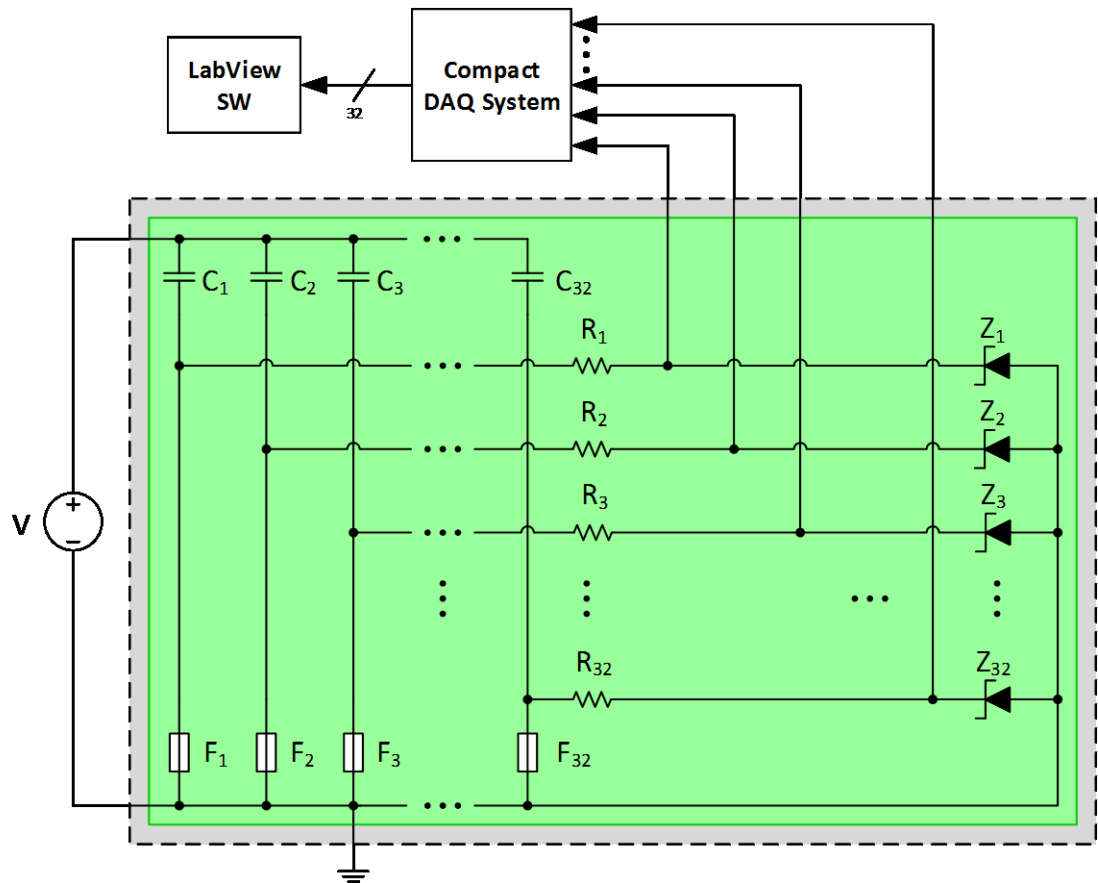
Figure 1. Schematic diagram of the accelerated test.

The test PCBs were mounted inside a climatic chamber where the ambient temperature was set at 140°C. The voltage of the DC power supply was selected to be six times the nominal voltage of the DUTs. Industrial-grade MLCCs by Murata of type X7R and package size 1210 were selected for the accelerated test. The voltage and capacitance rating of each capacitor was 25 V and 10 µF, respectively. To expose the ceramic grain boundaries, one cross-sectioned sample was selected for chemical etching and submerged in a solution of 95 mL distilled H2O, 3 mL HCl (32%) and 2 mL HF (40%) for 10 s. The thickness of the dielectric layer was measured with a Zeiss Sigma scanning electron microscope (SEM) to be 4.40 µm, and the average grain size was determined to be 0.35 µm. The internal electrode consisted of 418 layers. The ceramic grain boundaries and the dielectric thickness are shown in Figure 2a. A close-up picture of the ceramic grains is shown in Figure 2b.
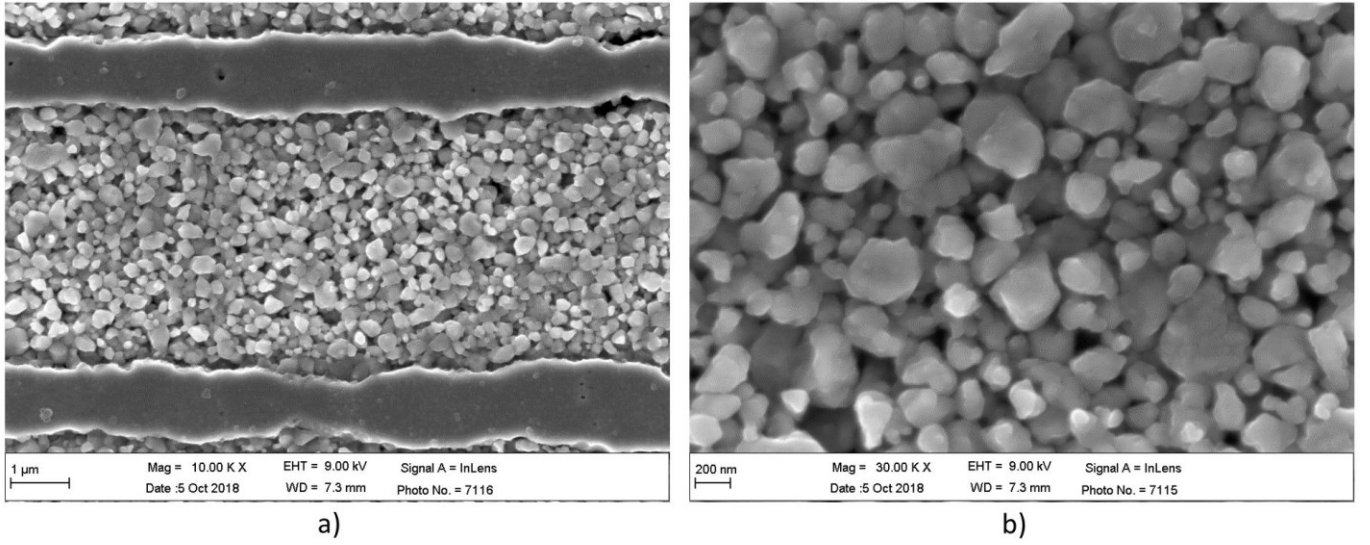
Figure 2. a) SEM image of the dielectric grain sizes between two electrodes in the MLCC and b) close-up image of the dielectric grains.

2.2. Analysis methods

After the test, the aged samples were scanned with a Phoenix Nanomex X-ray machine using both 2D and 3D X-ray imaging technologies. For the scans, the maximum detail detectability of the open nanofocus tube was 200 nm [13].

In 3D X-ray imaging, the samples were placed on a rotation stage between the radiation source and the image detector. Each sample was rotated 360° and 1000 2D X-ray images were taken. The images obtained were then reconstructed using datos|x 2 and VGStudio MAX software into a 3D model that can be sliced into multiple virtual cross-section images. The 3D model produced was utilized to analyse the failure location of the multilayer ceramic capacitors, as well as to evaluate the geometry and the volume of the insulation defect.

To verify the locations provided by the model with cross-section analysis, the samples were encapsulated into epoxy for structural support during the grinding. The exposed surface was ground gradually using an AccuStop precision grinding tool with silicon carbide grinding papers with grain sizes ranging from 320 to 4,000, with an accuracy of 20 μm. The final polishing was made using woven acetate polishing cloths and aluminium oxide polishing films combined with polycrystalline diamond lubricants with grain sizes of 9 μm, 3 μm and 1 μm. The results of the cross-sections were captured with a Keyence VHX-6000 optical microscope.

2.3. Measurement uncertainty analysis

The novelty of the proposed method of localizing dielectric breakdown using 3D X-ray imaging calls for an uncertainty analysis of the aforementioned approach. For the analysis, one MLCC was chosen as a calibrated workpiece and measured with a coordinate measurement machine (CMM) of the Hexagon TIGO SF type to obtain a calibrated value. In addition, an uncertainty analysis of the traditional cross-section approach is presented in order to compare the two methods.

The uncertainty of the dimensions measured by the 3D X-ray imaging method U_{3D} was determined according to the VDI/VDE 2630 part 2.1 standard [14] and given by

$$U_{3D} = k \cdot \sqrt{u_c^2 + u_d^2 + u_p^2 + u_b^2 + u_w^2}, \tag{1}$$

where k is the coverage factor, u_c is the standard uncertainty of measurement due to the uncertainty of calibration of the calibrated workpiece, u_d is the standard uncertainty of measurement due to the change (drift) in workpiece shape, u_p is the standard deviation of the repeated measurements, u_b is the standard measurement uncertainty of the correction of the systematic error, and u_w is the standard uncertainty of measurement due to variations in materials and production (e.g., coefficient of expansion, form errors and roughness) and calculated as

$$u_w = (t - 20°C) \cdot u_\alpha \cdot l. \tag{2}$$

The parameters in (1) were defined as follows: u_c was obtained from the ratio between the uncertainty of the CMM and the coverage factor, u_d was assumed to be negligible, u_p was obtained from the 3D model by repeatedly measuring the width of the calibrated workpiece, u_b was calculated as the difference between the mean value of the repeated measurements and the calibrated value obtained from the CMM.
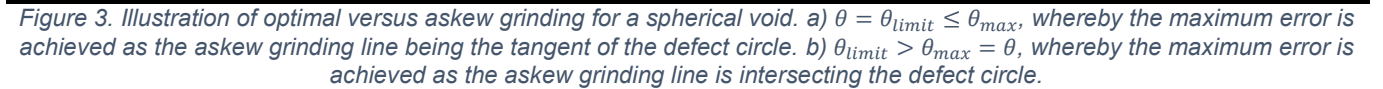
The combined uncertainty of the cross-section analysis U_{CS} was determined by identifying the prevailing uncertainty sources of the process and given by

$$U_{CS} = k \cdot \sqrt{u_{AccuS}^2 + u_{inst,K}^2 + u_{rep}^2 + u_\theta^2}, \tag{3}$$

where k is the coverage factor, u_{AccuS} is the standard uncertainty of the AccuStop grinding tool, $u_{inst,K}$ is the standard uncertainty of the optical microscope, u_{rep} is the standard deviation of the repeated measurements and u_θ is the standard uncertainty of the grinding angle.

The parameters in Eq. (3) were defined as follows: u_{AccuS} was neglected since the defects were large enough to always be revealed, $u_{inst,K}$ (with the installed optics and applied magnification) was estimated from the calibration data provided by the instrument, and u_{rep} was obtained by repeatedly measuring the width of the calibrated workpiece using the edge detection feature of the optical microscope.

The uncertainty caused by askew grinding was estimated based on a cross-sectional drawing of a faulted MLCC as shown in Figure 3, where the breakdown void is modelled as a circle V with a radius of r. Optimally executed grinding, parallel to the x-axis and with depth g, results in a line f_0, which is parallel to the y-axis and goes through the centre point of the void P_0. Slightly slanted grinding with an angle of θ, but with the same depth g, results in a line f_1 instead. With this grinding, P_1 is erroneously regarded as the centre of the void, whereby the error e is thus the difference between d_0 (the distance from the real centre of the void to the edge of the capacitor along f_0) and d_1 (the distance from P_1 to the edge of the capacitor along f_1). The distances were always measured to the closest edge, whereby d_0 and d_1 become d_0' and d_1', respectively, if $d_1 > d_1'$.

Figure 3. Illustration of optimal versus askew grinding for a spherical void. a) $\theta = \theta_{limit} \leq \theta_{max}$, whereby the maximum error is achieved as the askew grinding line being the tangent of the defect circle. b) $\theta_{limit} > \theta_{max} = \theta$, whereby the maximum error is achieved as the askew grinding line is intersecting the defect circle.

As shown in Figure 3a, the greatest possible θ at which the defect is still revealed, θ_{limit}, is defined by f_1 being the tangent of V at P_1. This represents the theoretical limit of a successful grinding, also resulting in the maximum error e_{max} with a given void location and radius. However, with some location and radius combinations, θ_{limit} grows impractically large regarding realistic grinding angles in the actual cross-section preparation process. For such combinations, a maximum grinding angle of two degrees, θ_{max}, was assumed. Thus, the maximum error is either achieved with θ_{limit}, or with θ_{max} if -$\theta_{limit} > \theta_{max}$. In the latter case, e_{max} is calculated based on Figure 3b, where the erroneously regarded centre of the void is in the middle of P_4 and P_5 – the points where the askew grinding line and the void circle intersect.

The maximum error is derived by first solving θ_{limit} for the given void location and radius with simple trigonometry as

$$(2g + r)\tan^2 \theta_{limit} + 2y_0 \tan \theta_{limit} + r = 0, \tag{4}$$

and, if $\theta_{limit} \leq \theta_{max}$, utilizing the equation of the askew grinding line expressed as

$$f_1(y, \theta) = y \tan \theta + x_0 - g \tan \theta \tan \frac{\theta}{2}, \tag{5}$$

in order to define P_2 and P_2', the intersections of f_1 and the MLCC edges. In the case of $\theta_{limit} > \theta_{max}$, f_1 is determined by first solving the intersections P_4 and P_5 as the roots in

$$(y - y_0)^2 + (f_1(y, \theta) - x_0)^2 - r^2 = 0. \tag{6}$$

Utilizing the coordinates of the intersections, the maximum error for a given void location and radius is calculated as

$$e_{max} = \begin{cases} \left| (l - y_0) - \sqrt{(y_0 - r\sin\theta_{limit} - y_2)^2 + (x_0 + r\cos\theta_{limit} - x_2)^2} \right| & ,\theta_{limit} \leq \theta_{max} \; \forall \; d_1 \leq d_1' \\[12pt] \left| y_0 - \sqrt{(y_0 - r\sin\theta_{limit} - y_2')^2 + (x_0 + r\cos\theta_{limit} - x_2')^2} \right| & ,\theta_{limit} \leq \theta_{max} \; \forall \; d_1 > d_1' \\[12pt] \left| (l - y_0) - \sqrt{\left(\dfrac{y_5 + y_4}{2} - y_2\right)^2 + \left(\dfrac{x_5 + x_4}{2} - x_2\right)^2} \right| & ,\theta_{limit} > \theta_{max} \; \forall \; d_1 \leq d_1' \\[12pt] \left| y_0 - \sqrt{\left(\dfrac{y_5 + y_4}{2} - y_2'\right)^2 + \left(\dfrac{x_5 + x_4}{2} - x_2'\right)^2} \right| & ,\theta_{limit} > \theta_{max} \; \forall \; d_1 > d_1' \end{cases} \tag{7}$$

Finally, if we assume that the grinding angle is uniformly distributed between 0 and $\theta \in \{\theta_{limit}, \theta_{max}\}$, the standard uncertainty is achieved as

$$u_\theta = \frac{e_{max}}{\sqrt{3}} \tag{8}$$

In addition, with a spherical void, the AccuStop grinding tool may also cause errors if the grinding is executed askew, and this would be seen as a vertical displacement of the grinding line f_1. However, in cases where the defect is revealed, the displacement can only move f_1 downwards and thereby reduce the error. Thus, the greatest error with a given location and radius is achieved with θ_{limit}, whereby the error caused by the AccuStop can be omitted. For very small defects, this assumption may not be valid, since there is a risk that the defect will be lost due to excessive grinding, or not revealed due to insufficient grinding. In this study, however, the defects proved large enough to always be revealed, whereby the aforementioned assumption can be made.

3. Results and discussion

Sixty-four of the aged samples in this study were first investigated using the 2D X-ray imaging method as described in [12]. It was observed that the dielectric breakdown defects could not be easily detected with this method, mainly due to their small size and the limited tilting angle of the flat panel detector. The only anomaly seen with 2D X-ray imaging was in Sample 9, which is shown in Figure 4a. The 2D X-ray image was taken with a tube voltage of 130 kV and current of 100 μA.

With 3D X-ray imaging, there are no viewing angle restrictions, since the samples can be rotated 360 ° around any axis. Thirty-two of the aged samples were imaged with this method. For each capacitor, the X-ray tube voltage and current was set to 130 kV and 102 μA. The image acquisition time was set to 1000 ms, and 1000 2D X-ray images were taken, which resulted in a scanning time of one hour and seven minutes. These settings provided virtual cross-section images with sufficient accuracy for detecting dielectric breakdown in the 3D model in over 90 percent of the samples analysed. In the case of Sample 9, the precise location of the dielectric breakdown near the interface of the active area and the ceramic body was revealed in the 3D model, as indicated by the red arrow in Figure 4b. The anomaly seen in the 2D X-ray image, is indicated by the blue arrow.
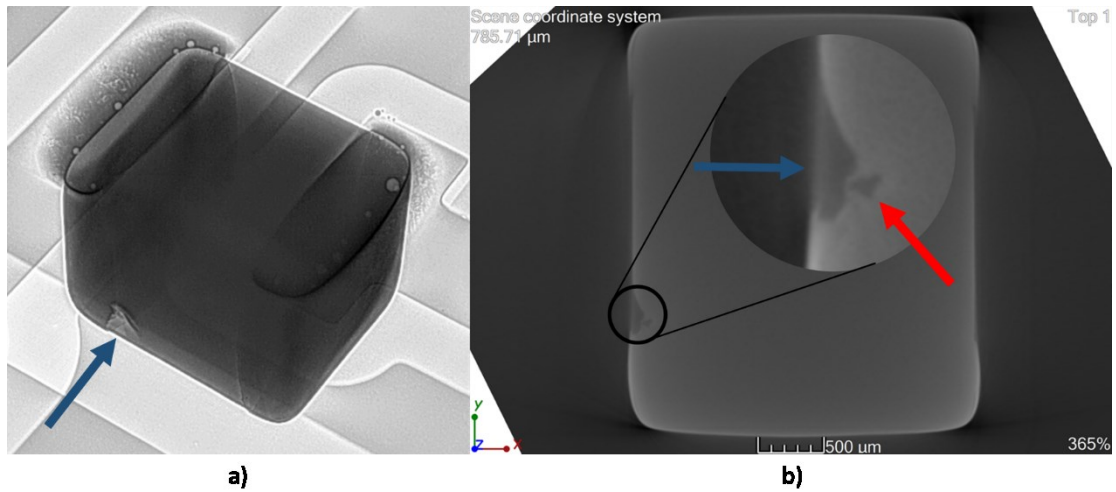
Figure 4. 2D and 3D X-ray images of the same multilayer ceramic capacitor. a) the anomalies are located at the surface of the ceramic capacitor body indicated by blue arrow. The white anomalies in the solder joints are voids. b) dielectric breakdown was only revealed by virtual cross-section scan of the 3D X-ray model, indicated by the red arrow (For interpretation of the references to colour in this figure legend, the reader is referred to the web version of this article).

Figure 5 shows a virtual 3D X-ray scan of one multilayer ceramic capacitor that failed in dielectric breakdown during the aging test. Dielectric breakdowns, visible as dark spots, were found in 30 of the 32 samples that failed during the test. Figures 5a–c represent the virtual 2D slice through the breakdown location, where a) represents a top-down view, b) the view perpendicular to the terminal, and c) the view perpendicular to the side of the capacitor soldered onto the test PCB. Figure 5d illustrates the capacitor in respect to the coordinate system with origin in the centre.
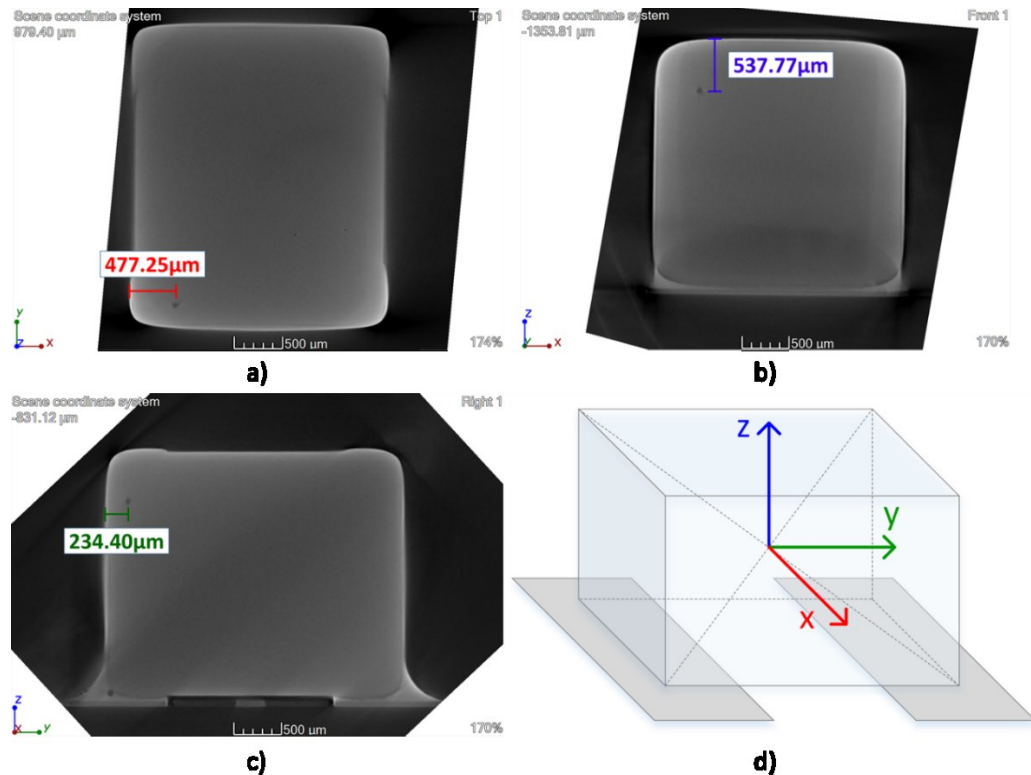

Figure 5. The locations of the dielectric breakdown using 3D X-ray imaging. a) the location of the defect in a top-down view; b) the location of the defect from the view of the end termination; c) the location of the defect according to the side view of the capacitor. d) illustrates the capacitor according to the coordinate system with origin in the centre.

To assess the location and to verify dielectric breakdown failure, a physical cross-section of the sample shown in Figure 5 was prepared. The sample was ground perpendicular to the x-axis to expose the alternately stacked layers of the internal electrodes. Based on the 3D X-ray measurements (see Figure 5) the grinding depth was set to 470 µm with an additional polishing of 10 µm, whereby the defect was revealed. The measurements along the y- and z-axes based on the physical cross-section were 233.99 µm and 538.63 µm, respectively, which also corresponded to the measurements obtained from the 3D X-ray model in Figure 5.

The results of the cross-section and comparison to the 3D X-ray analysis are presented in Figure 6. As seen in Figure 6c and 6d, molten dielectric and nickel electrodes were found at the damage site, which strongly supports that a dielectric breakdown had occurred. The red arrows indicate molten nickel bridging of the neighbouring electrodes.
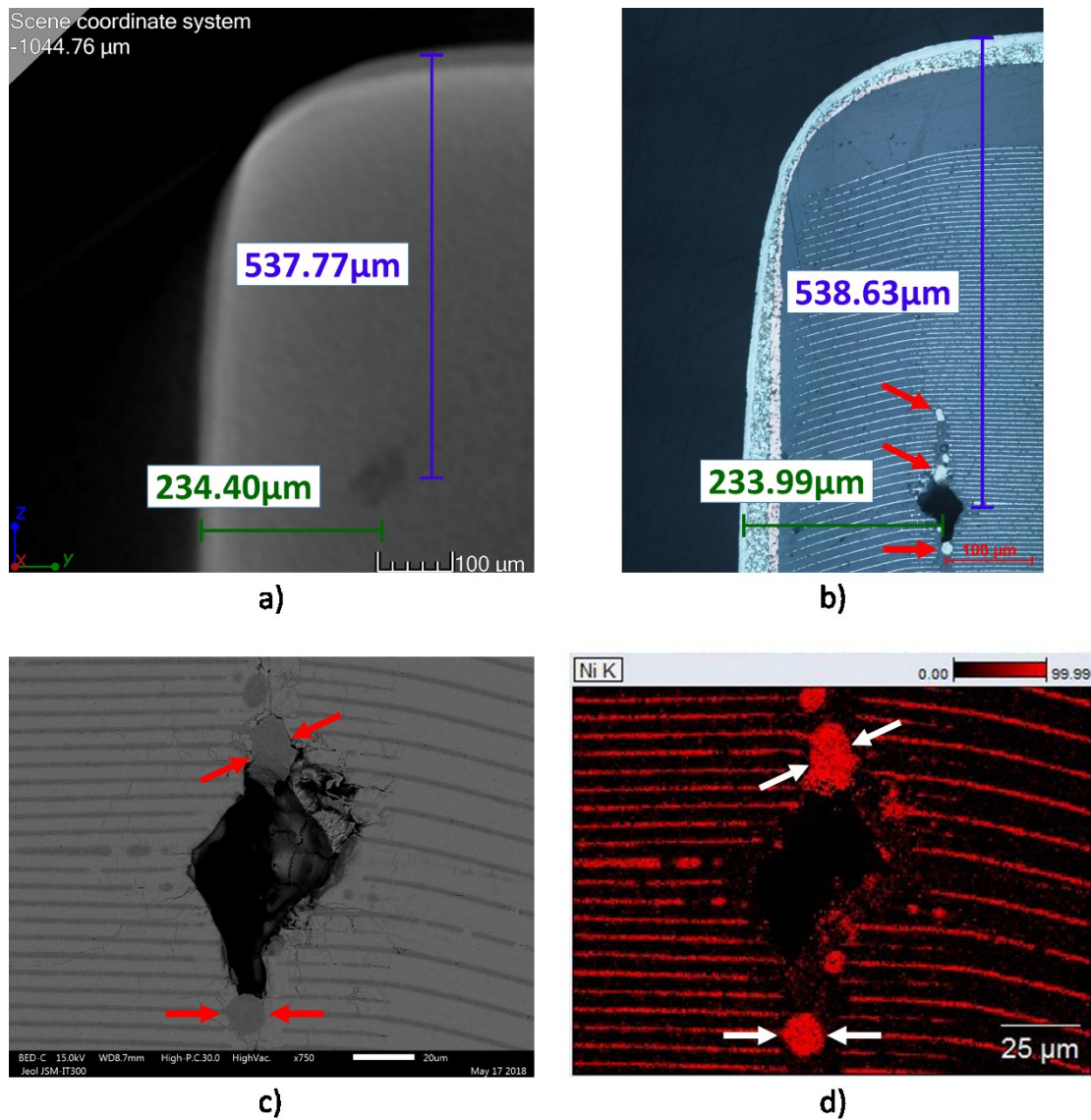

Figure 6. Comparison between 3D X-ray analysis and cross-sectioning. a) measurements along the z- and y-axes obtained from the 3D model; b) corresponding measurements obtained from cross-section analysis. The red arrow indicates the molten internal electrodes which were electrically shorted. c) SEM image of the damage site; d) energy dispersive X-ray image of the molten nickel that was shorted (For interpretation of the references to colour in this figure legend, the reader is referred to the web version of this article).

In Figure 7a and 7b, all 30 dielectric breakdown locations from the 3D X-ray imaging were plotted in scatter graphs with the same coordinate system as in Figure 5d. The grey box represents the dimensions of the MLCC. Figure 7a presents a top-down view and Figure 7b a view perpendicular to the end terminal of the ceramic capacitor. In order to verify the dielectric breakdowns and the locations provided by the 3D X-ray imaging, ten MLCCs were prepared by cross-sectioning. By grinding the measured length along the x-axis, the defect was always revealed as a void surrounded by molten dielectric and nickel electrodes. This phenomena were observed at the damage site in all of these ten samples. The selected samples are marked with a red hexagram in the scatter plots.

In order to compare the accuracy of the 3D X-ray imaging and the cross-section analysis in localizing the dielectric breakdown voids, an uncertainty analysis was performed for the ten selected samples as presented in section 2.3. The results are shown separately for the y- and z-axes in Figures 7c), 7e), and 7d), 7f) respectively. It can be noticed that the uncertainty in the cross-section analysis, indicated by the red error bars in the middle subplots, is greater for each sample compared to the uncertainty in the 3D X-ray imaging, indicated by the blue bars. Therefore, it can be concluded that 3D X-ray imaging is more accurate in locating dielectric breakdown defects than cross-section analysis only. Moreover, as seen in the lowermost subplots, the absolute differences of the measured defect centre locations between the two methods are within a few microns.
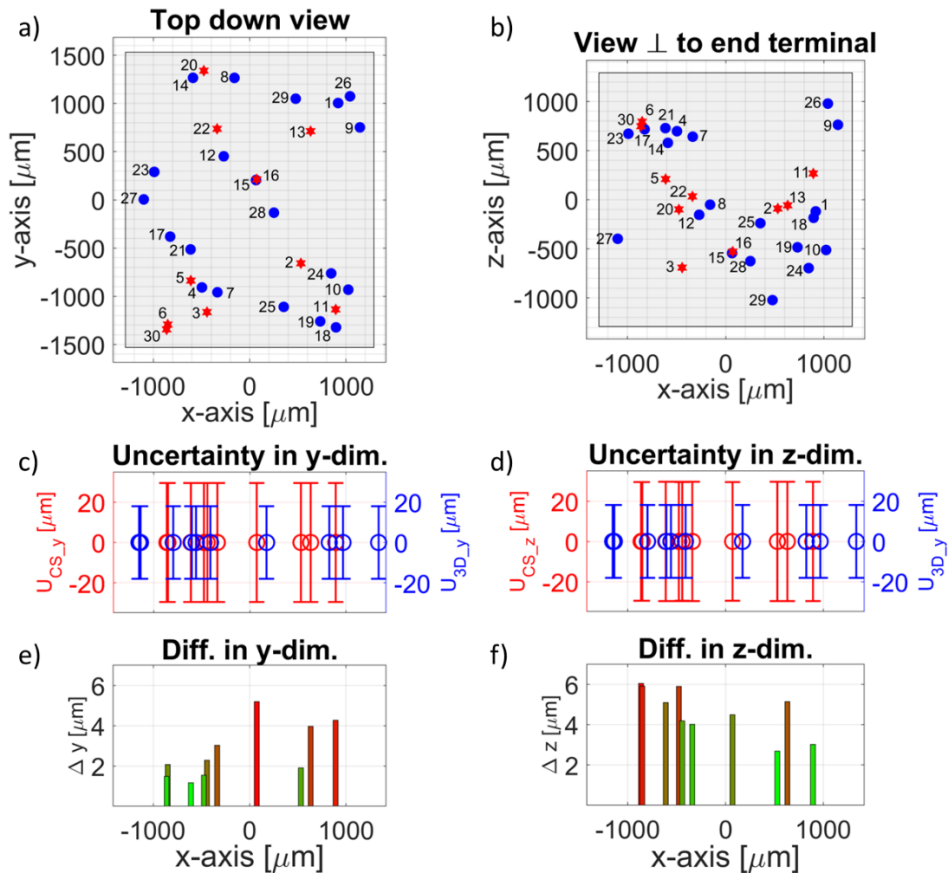

Figure 7. Scatter plots of the dielectric breakdown locations in 30 DUTs from 3D X-ray imaging. The samples selected for cross-section and 3D X-ray comparison are marked with a red hexagram, while the sample locations marked by blue dots are the rest of the defect locations detected with 3D X-ray imaging. a) the location of the defects from a top-down view; b) the locations of the defects from the end termination view of the MLCC. The uncertainty in cross-section (red) and in 3D X-ray imaging (blue) are shown for the y- and z-dimensions in c) and d). The absolute difference of the defect centres between the measurement methods are shown for the y- and z-dimensions in d) and f), where larger differences are in red and smaller in green (For interpretation of the references to colour in this figure legend, the reader is referred to the web version of this article).

In an effort to further explore the advantages provided by 3D X-ray imaging, the defect in Figure 6 was studied by virtually cross-sectioning the model through the middle of the defect. The resulting image is presented in Figure 88a, where the void was measured to be 51.27 µm and 64.85 µm respectively. From the cross-section analysis in Figure 88b, the width was measured to be 49.93 µm and the height to be 70.38 µm, which corresponds well to the 3D measurements. The uncertainty in these measurements remains the same, 18 µm, for the 3D X-ray imaging method. However, for the cross-section method, the uncertainty is now reduced to 6-µm due to the increase in accuracy of the VHX as a result of increased magnification.
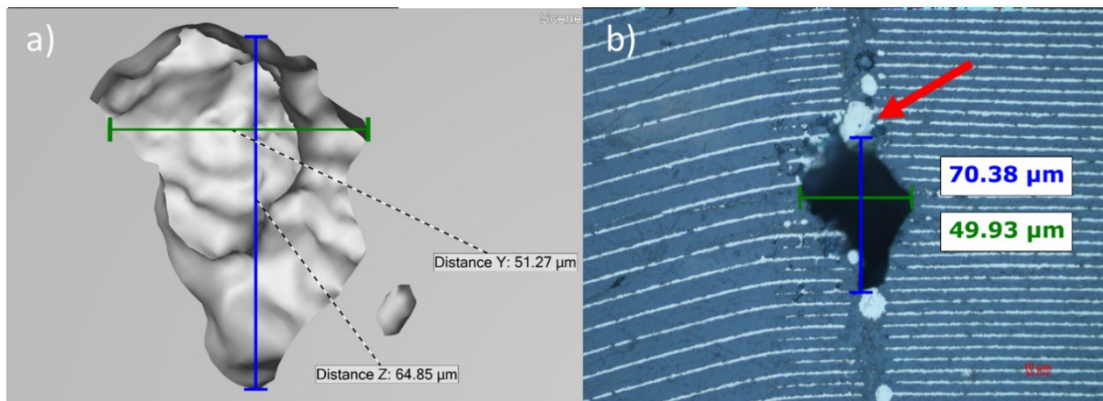

Figure 8. Comparison between 3D X-ray imaging and cross-sectioning of the size of the void. a) measurements along the z- and y-axes obtained from 3D model; b) corresponding measurements obtained from cross-sectioning analysis. The red arrow indicates the molten internal electrodes that were electrically shorted.

Additional options provided with 3D X-ray imaging are the possibilities to investigate the distribution of the defect locations as well as the volume of the dielectric breakdown void inside the MLCC. For instance, it can be seen from the scatter graph in Figure 7, that the defects were randomly distributed for this sampling of aged MLCCs. The volume of the void shown in Figure 8 could be estimated at 106,700 µm^3 using VGStudio analysis software. The result of the volume analysis is presented in Figure 99. Hence, 3D X-ray imaging provides an opportunity to obtain more information about different dielectric failure modes for future research.
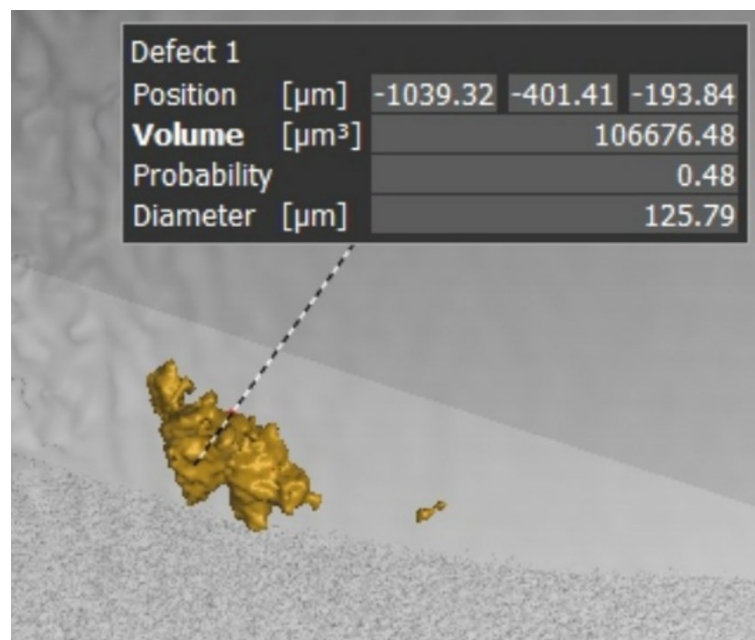

Figure 9. Calculated volume of the defect with VGStudio.

When considering cavity volume estimation of dielectric breakdowns within MLCCs, a short is first required to bridge two neighbouring electrodes. Consequently, a minimum condition for at least one dimension of the resulting failure site is defined by the thickness of the dielectric layer, measured as 4.4 μm in the investigated MLCCs. However, in this study, the dimensions of the smallest void measured from the 3D models was 19.5 μm along the y-axis, 19.6 μm along the z-axis and 24.3 μm along the x-axis and detected without difficulties. Based on the uncertainty analysis, cavity dimensions smaller than 18 μm would not be detectable with this X-ray system. This corresponds well with the observations made in this study.

The applicability of the presented method in multilayer ceramic capacitors originates from the significant difference in the material densities of the ceramic and the defect cavity. Thus, the proposed method has the potential to be applicable for investigating breakdown defects in other ceramic components such as metal oxide varistors and ceramic disc capacitors.

Considering future research, an interesting and closely related topic is the feasibility of this method for detection and investigation of microcracks in ceramic materials. Possible applications are for example: detection of conchoidal cracks in ceramic substrates after the ultrasonic welding process and porosity analysis of ceramic materials. In the latter, more specifically, to determine of the closed pore size distribution which is not easily defined using the conventional mercury penetration porosimetry technique. The proposed method could also be appropriate for detecting delamination between the ceramic substrate and the interfacing layers in components such as surface-mount resistors and piezo actuators.

Conclusion

In conclusion, the feasibility of 3D X-ray imaging to easily localize small dielectric breakdown defects in multilayer ceramic capacitors with submicron accuracy and without destructive effects was demonstrated. Compared to physical cross-section analysis, 3D X-ray imaging is more accurate in detecting dielectric breakdown locations in MLCCs. On the other hand, a physical cross-section is more accurate in determining the size of the defect; however, the location provided by the 3D X-ray imaging is useful for this task as well. Another advantage of 3D X-ray imaging over cross-section analysis is the reduced time required to localize the dielectric breakdown region. By implementing 3D X-ray imaging in the failure analysis process, succeeding in sample preparation with cross-sectioning becomes a straightforward task, as the exact grinding depth is provided beforehand. Moreover, a precise amount of material can be removed to reveal the breakdown region with minimal risk of accidentally losing failure evidence during the process. Lastly, it was observed that 3D X-ray imaging can detect dielectric breakdown locations in MLCCs that may not be detected using only 2D X-ray imaging.

For future research, the distribution of defects inside an MLCC of a sampling can be easily assessed with 3D X-ray imaging. In this study, the defects in the selected sampling were randomly distributed. The proposed method also allows for volume approximation of the dielectric breakdown void, which may contribute to new insight of failure mechanisms in MLCCs.

Acknowledgement

References

[1] J. Gu, M.H. Azarian, M.G. Pecht, Failure prognostics of multilayer ceramic capacitors in temperature-humidity-bias conditions, Proceedings of the 1st International Conference on Prognostics and Health Management, (2008), pp. 1–7.

[2] F. Yeung, Y.C. Chan, Electrical failure of multilayer ceramic capacitors caused by high temperature and high humidity environment, Proceedings 44th Electronic Components and Technology Conference, (1994), pp. 847–853.

[3] J. Yoon, K. Lee, S. Lee, Analysis the reliability of multilayer ceramic capacitor with inner Ni electrode under highly accelerated life test conditions, Trans. Electr. Electron. Mater. 10 (1) (2009) 5–8.

[4] D. Liu, M.J. Sampson, Some aspects of the failure mechanisms in BaTiO3-Based multilayer ceramic capacitors, Proc. CARTS Int. (2012) 59–71.

[5] D. Liu, M.J. Sampson, Reliability evaluation of base-metal-Electrode multilayer ceramic capacitors for potential space applications, Proc. CARTS Int. 45 (2011) -63.

[6] M. Bâzu, T. Bǎjenescu, Failure Analysis: A Practical Guide for Manufacturers of Electronic Components and Systems, first ed., John Wiley & Sons Ltd, Chichester, 2011.

[7] N. Blattau, C. Hillman, Design Guidelines for Ceramic Capacitors Attached With SAC Solder, DfR Solutions College Park. http://resources.dfrsolutions.com/Publications/2005-2007/2006_DesignCeramCapSAC.pdf (Accessed 04 November 2017).

[8] R.J. Weachock, D. Liu, Failure Analysis of Dielectric Breakdowns in Base-Metal Electrode Multilayer Ceramic Capacitors, Proc. CARTS Int. (2013) 151–165.

[9] W. Minford, Accelerated life testing and reliability of high K multilayer ceramic capacitors, Ieee Trans. Compon. Hybrids Manuf. Technol. 5 (3) (1982) 297–300.

[10] D. Liu, Highly accelerated life stress testing (HALST) of base-metal electrode multilayer ceramic capacitors, Proc. CARTS Int. (2013) 235–248.

[11] J. Kim, et al., Degradation behaviors and failure analysis of Ni-BaTiO3 base-metal electrode multilayer ceramic capacitors under highly accelerated life test, Curr. Appl. Phys. 10 (5) (2010) 1297–1301.

[12] C. Andersson, et al., Detection of cracks in multilayer ceramic capacitors by X-ray imaging, Microelectron. Reliab. (2016) 352–356.

[13] https://www.gemeasurement.com/inspection-ndt/radiography-and-computedtomography/phoenix-nanomex, (accessed 25 November 2017).

[14] VDI/VDE 2630-2.1 standard, Computed Tomography in Dimensional Measurement - Determination of the Uncertainty of Measurement and the Test Process Suitability of Coordinate Measurement Systems With CT Sensors, (2012).